IOP Publishing Journal of Physics D: Applied Physics
J. Phys. D: Appl. Phys. **52** (2019) 465301 (8pp) https://doi.org/10.1088/1361-6463/ab3953

Bending and interlayer shear moduli of ultrathin boron nitride nanosheet

Wenyang Qu[1], Soumendu Bagchi[2], Xiaoming Chen[3], Huck Beng Chew[2,5] and Changhong Ke[1,4,5]

[1] Department of Mechanical Engineering, State University of New York at Binghamton, Binghamton, NY 13902, United States of America
[2] Department of Aerospace Engineering, University of Illinois at Urbana-Champaign, Urbana, IL 61801, United States of America
[3] State Key Laboratory for Manufacturing Systems Engineering, Micro- and Nanotechnology Research Center, Xi'an Jiaotong University, Xi'an, Shaanxi 710049, People's Republic of China
[4] Materials Science and Engineering Program, State University of New York at Binghamton, Binghamton, NY 13902, United States of America

E-mail: cke@binghamton.edu and hbchew@illinois.edu

Received 11 June 2019, revised 31 July 2019
Accepted for publication 7 August 2019
Published 29 August 2019

Abstract

We investigate the bending rigidity of ultrathin hexagonal boron nitride nanosheet (BNNS) through quantifying its self-folded conformations on flat substrates by using atomic force microscopy and atomistic simulations. The bending stiffness of two to six layers of BNNS is found to follow a power function of its thickness with a power index of ~2.35 and is substantially higher than that of comparable graphene. In contrast, monolayer graphene possesses a higher stiffness than its h-BN counterpart. We attribute the high bending stiffness of multilayer BNNS to its partially ionic B–N bondings and corrugated electronic structures, which result in one order of magnitude stronger interlayer shear interaction in h-BN than in graphene. The higher out-of-plane bending and interlayer shear rigidities suggest that unlike graphene, BNNS is less prone to interlayer delamination-induced structural inhomogeneities (e.g. shearing, rippling and kinks) and thus is suitable as a building block for atomically thin electronics and a reinforcing filler for nanocomposites.

Keywords: boron nitride nanosheet, bending stiffness, interlayer shear modulus, atomic force microscopy, atomistic simulations

(Some figures may appear in colour only in the online journal)

1. Introduction

The out-of-plane bending deformability of two-dimensional (2D) nanomaterials, such as graphene and hexagonal boron nitride nanosheet (BNNS), controls many of their fundamental mechanical and physical properties and is of paramount importance to their potential engineering applications [1–4]. Structurally, 2D materials are layered nanocrystals consisting of one or more stacked sheets that are single atom thick. The bending rigidity of monolayer 2D materials is simply governed by the underlying chemical bond stretching/compression/rotation behaviors of atoms within the single atomic sheet [5]. For multilayer 2D materials, however, the bending rigidity becomes more complicated due to the added contributions of interlayer interactions [6]. The bending rigidities of monolayer and few-layer graphene have been extensively studied [7–18]. Studies reveal that weak interlayer interactions in graphene, associated with pure van der Waals interactions, control its bending deformability through a series of structural inhomogeneities, such as interlayer shearing/sliding, and the formation of delamination-induced ripples and kinks [18]. In contrast, hexagonal BNNS possesses much stronger interlayer interactions than graphene [19], which is ascribed to its partially ionic B–N bonding and the resulting

[5] Author to whom any correspondence should be addressed.

corrugated electronic structure [20]. However, a quantitative understanding of how the stronger interlayer interactions contribute to the overall bending deformability of thin hexagonal BNNS remains elusive.

Here, we investigate the bending rigidity of two to six layers of BNNS by quantifying its self-folded conformations on flat substrates using atomic force microscopy (AFM) in combination with nonlinear continuum mechanics modeling and atomistic simulations. We show that the bending rigidity of few-layer BNNS is significantly higher than that of its graphene counterpart, due to the order of magnitude higher interlayer shear modulus of h-BN versus graphene.

2. Results and discussion

2.1. Experimental characterization of self-folded BNNS flakes by using AFM

The BNNS flakes employed in this study were separated from boron nitride microplatelets (Momentive Performance Materials Inc.) using mechanical cleavage methods [21] and then transferred onto flat silicon oxide substrates. BNNS flakes were subsequently inspected at ambient environment inside a high-resolution AFM (XE-70 from Park Systems operating in tapping mode [22]) and a Raman microscope (Renishaw inVia with a laser of 532 nm in wavelength). The employed silicon AFM probes, which were purchased from Budget Sensors, possess a nominal spring constant of 40 N m^{-1} and a nominal resonant frequency of 300 kHz. A free amplitude of 1200 nm and a set-point amplitude of 500 nm were used in tapping mode AFM. A small percentage of thin BNNS flake samples (less than 3 nm in height) were identified to stay in self-folded conformations, as exemplified by the self-folded BNNS flake shown in figure 1(a). The AFM image contrast further shows that this BNNS flake is composed of multiple thickness domains. The AFM height profile as displayed in figure 1(b) reveals the respective heights of those distinct domains along the marked blue-dashed line in figure 1(a) with respect to the substrate baseline. Considering that h-BN possesses an interlayer separation distance of $t_0 = 0.34$ nm, the four exhibited domains from left to right are concluded to be monolayer (1L), bilayer (2L), trilayer (3L), and six-layer (6L), respectively. It is noted that the measured heights of the BNNS domains by AFM are all noticeably higher than their theoretical thicknesses that are calculated by the number of layers and the h-BN interlayer distance. This discrepancy can be attributed to several factors, including the surface roughness of the substrate and the artifact caused by the AFM tip-sample interaction [23]. The 6L domain is further identified as a self-folded domain based on the existence of a prominent hump on the domain edge that possesses a relative height of about 1.33 nm with respect to the top surface of the flipped segment as well as approximately the same thickness for both the underlying and the flipped segments. This self-folded domain likely resulted from tearing and folding of the initially flat 3L domain either mechanically during the sample preparation/transfer process [24] and/or thermodynamically through a self-assembly process [25]. The mirrored white-dashed lines in figure 1(a) mark the approximate position of the flipped segment in its flat conformation. It is noted that the assigned numbers of layers (N) of the BNNS domains based on AFM height measurements are confirmed with the Raman spectroscopy measurements, which are displayed in figure 1(c). The measured G band (E_{2g}) mode peak frequency and the FWHM (full width at half maximum) bandwidth for 2L to 6L BNNS are consistent with prior studies [20, 21]. The hump height at the folded domain edge is an important parameter in evaluating the bending stiffness of the underlying BNNS flake. We characterized a number of self-folded BNNS domains that were formed by BNNS flakes of two to six layers and the measurements of their hump heights are presented in figure 1(d), which displays a linear-increasing trend between the hump height and the number of layers in BNNS (and consequently its thickness).

2.2. Quantification of the bending stiffness and interlayer shear modulus of BNNS using nonlinear continuum mechanics modeling

The elastic deformations of low-dimensional nanomaterials, such as those made of B–N and C–C bonds, have been elucidated using continuum mechanics theories and molecular dynamics (MD) simulations [26, 27]. We extract the equivalent bending stiffness of BNNS from AFM measurements of its self-folded conformation using a nonlinear mechanics model illustrated in figure 2(a). In this model, multilayer BNNS is treated as a non-stretchable solid elastic sheet subjected to pure bending and the red curve in figure 2(a) represents its middle-plane (neutral-plane) deformation curvature in a self-folded conformation, which consists of two delamination points, i.e. the peel front at point A and the heal front at point B. The equilibrium of the folded BNNS sheet is given as

$$D_{\mathrm{m}}\frac{d^2\theta}{ds^2} = P\sin(\alpha-\theta), \tag{1}$$

where s is the length of the curve from the heal front B; θ is the rotation angle; D_{m} is the bending rigidity of the sheet; P and α are the internal force in the sheet and its orientation angle with respect to the deformation slope of the sheet, respectively. The boundary conditions are the deformation curvatures at the two delamination fronts that are given as $(d\theta/ds)_{\mathrm{A}} = \sqrt{2W_{\mathrm{BN-Sub}}/D_{\mathrm{m}}}$ for the peeling front and $(d\theta/ds)_{\mathrm{B}} = \sqrt{2W_{\mathrm{BN-BN}}/D_{\mathrm{m}}}$ for the heel front, in which $W_{\mathrm{BN-Sub}}$ is the adhesion energy per unit area between the BNNS and the substrate and $W_{\mathrm{BN-BN}}$ is the adhesion energy per unit area between two adhered BN sheets in the flat-healed domain with an equilibrium distance $d = N \times t_0$. For BNNS of two or more layers, these two adhesion energy terms are estimated as $W_{\mathrm{BN-Sub}} = 2\sqrt{\gamma_{\mathrm{sub}}\cdot\gamma_{\mathrm{BN}}}$ and $W_{\mathrm{BN-BN}} = 2\gamma_{\mathrm{BN}}$, in which γ_{sub} and γ_{BN} are surface energies of the substrate and h-BN, respectively. By considering $\gamma_{\mathrm{sub}} = 115$ mJ m^{-2} for silicon dioxide [28] and $\gamma_{\mathrm{BN}} = 233$ mJ m^{-2} [29], $W_{\mathrm{BN-Sub}}$ and $W_{\mathrm{BN-BN}}$ are calculated to be about 328 mJ m^{-2} and 467 mJ m^{-2}, respectively, which, for simplicity, are assumed to be constants for the few-layer BNNS examined here. The deformation profile of the folded sheet at equilibrium can be

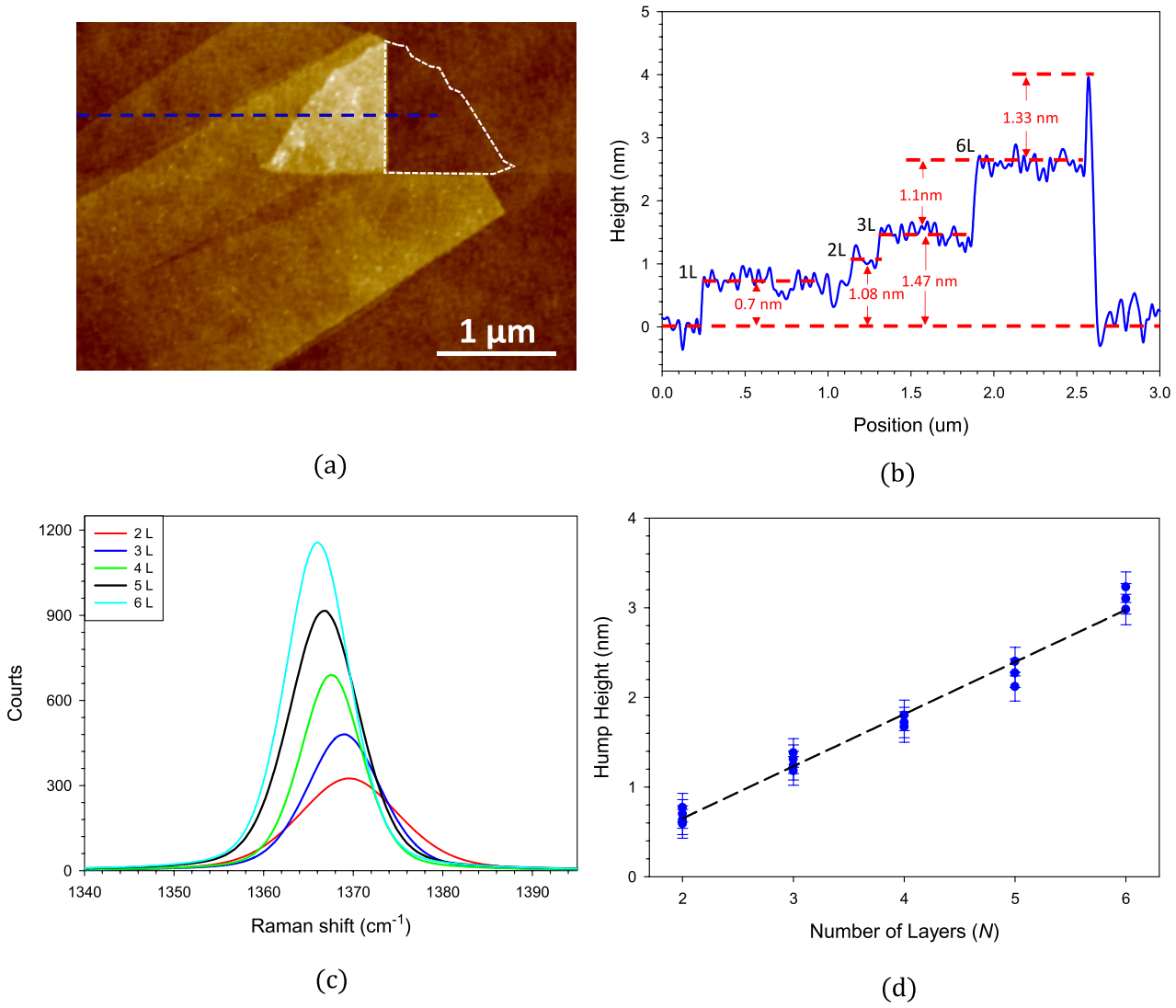

Figure 1. (a) AFM image of one self-folded BNNS flake. The white-dashed lines indicate the possible initial flat position of the folded segment. (b) AFM line topography profile of the BNNS flake in (a) along the marked blue line. (c) Representative Raman spectra of 2L–6L BNNS. (d) The measured hump height of self-folded BNNS flakes with a linear fitting curve (dashed line).

determined by solving equation (1) with the aid of boundary conditions.

The bending stiffness of BNNS D_m is obtained by means of matching the predicted hump height to the measured value (figure 1(d)). Figure 2(b) shows the calculated bending stiffness of 2–6L BNNS (red empty squares), which are also summarized in table 1 and can be well fitted by using a power function of its thickness that is given as $D_m(\text{eV}) = 15.8[N \times t_0(\text{nm})]^{2.35}$. For comparison, figure 2(b) also includes a plot of previously reported bending stiffness data (black empty circles) for few-layer graphene that were obtained using a similar method as the present study [16]. It can be clearly seen that the bending stiffness of few-layer BNNS is consistently much higher than that of comparable graphene, which is in contrast to monolayer h-BN (0.95 eV) [17] that reportedly possesses a lower stiffness than monolayer graphene (1.2–1.4 eV) [5, 30]. To the best of our knowledge, this study reports, *for the first time*, quantitative experimental measurements of the bending rigidity of thin BNNS. Figure 2(c) displays the theoretically predicted middle-plane deformation profiles of self-folded few-layer BNNS, based on our experimentally derived average bending stiffness values summarized in table 1.

The above findings suggest that interlayer interaction in h-BN is strong and has a substantial influence on the bending rigidity of multilayer BNNS. We quantify the interlayer shear interaction in h-BN using an energy method [11]. The total strain energy in a self-folded N-layer sheet, which is the bending energy if the N-layer sheet is considered as a one-piece structure, equals the summation of the bending energy in each sheet and the shear strain energy in each interlayer, which is given as [11, 16]

$$\frac{D_m}{2}\int_0^l \left(\frac{d\theta}{ds}\right)^2 ds = \frac{D_s}{2}\sum_{i=1}^{N}\int_0^l k_i^2 ds + \frac{(N-1)Gt_0}{2}\int_0^l \left(\tan^{-1}\theta\right)^2 ds, \quad (2)$$

where D_s is the bending stiffness of monolayer h-BN, G is the interlayer shear modulus of h-BN, and k_i is the bending curvature of each BN sheet and is calculated by using the

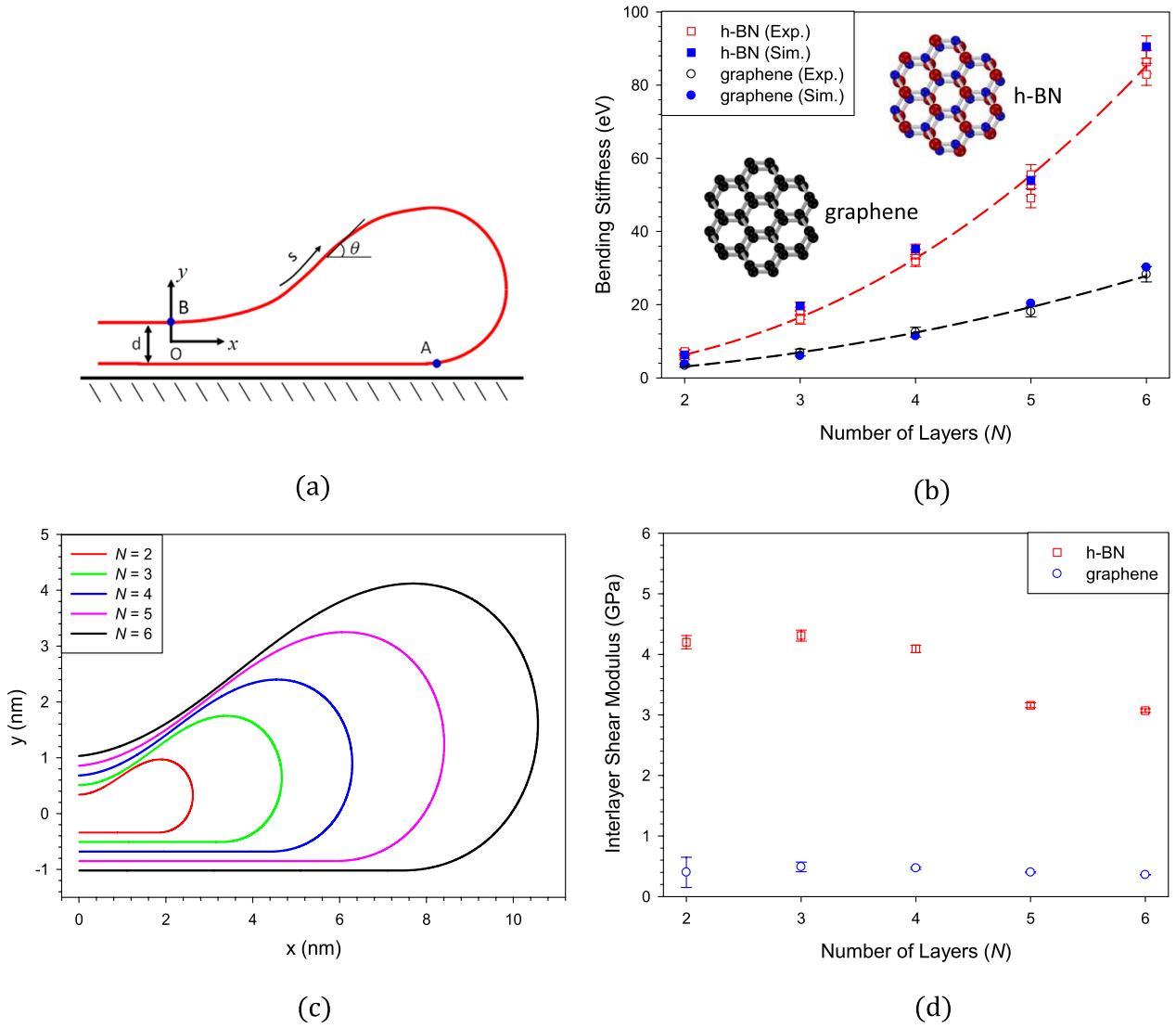

Figure 2. (a) Schematic of the 1D continuum mechanics model of self-folded BNNS. (b) The comparison of the experimental measurements and molecular simulations of the bending stiffness of few-layer BNNS (experiment—empty square; simulation—solid square) and graphene (experiment—empty circle; simulation—solid circle). Inserts are schematics of bilayer h-BN and graphene. (c) Theoretically predicted neutral-plane deformation profiles of self-folded 2L to 6L BNNS. (d) The calculated interlayer shear modulus of h-BN and its comparison with the values reported for graphene. The experimental values of graphene in (b) and (d) are from [16].

Table 1. Summary of experimental measurements and simulations of the bending stiffness (in eV) of h-BN and graphene (the experimental values of graphene are from [16]).

	h-BN		Graphene	
No. of layers	Experiments	Simulations	Experiments	Simulations
1	—	0.86	—	1.40
2	6.15 ± 0.61	6.32	3.35 ± 0.43	3.76
3	17.69 ± 1.24	19.65	6.92 ± 0.94	6.05
4	33.59 ± 1.35	35.28	12.50 ± 1.34	11.45
5	50.78 ± 2.62	54.00	18.10 ± 1.45	20.33
6	86.26 ± 3.05	90.53	28.29 ± 2.08	30.21

theoretically predicted self-folding profiles (figure 2(c)). By considering $D_s = 0.95$ eV [17], the interlayer shear modulus of 2–6L BNNS is calculated by using equation (2) and is found to be within the range of 3.07–4.31 GPa (figure 2(d)), which is consistent with the prior *ab initio* data for h-BN (2.6–5.1 GPa) [31], but is much higher than prior values reported for graphene (0.19–0.49 GPa) [9–11, 16]. The findings of the interlayer shear modulus of h-BN, which is close to one order of magnitude higher than that of graphene, indicate that the strong interlayer interaction substantially stiffens multilayer BNNS.

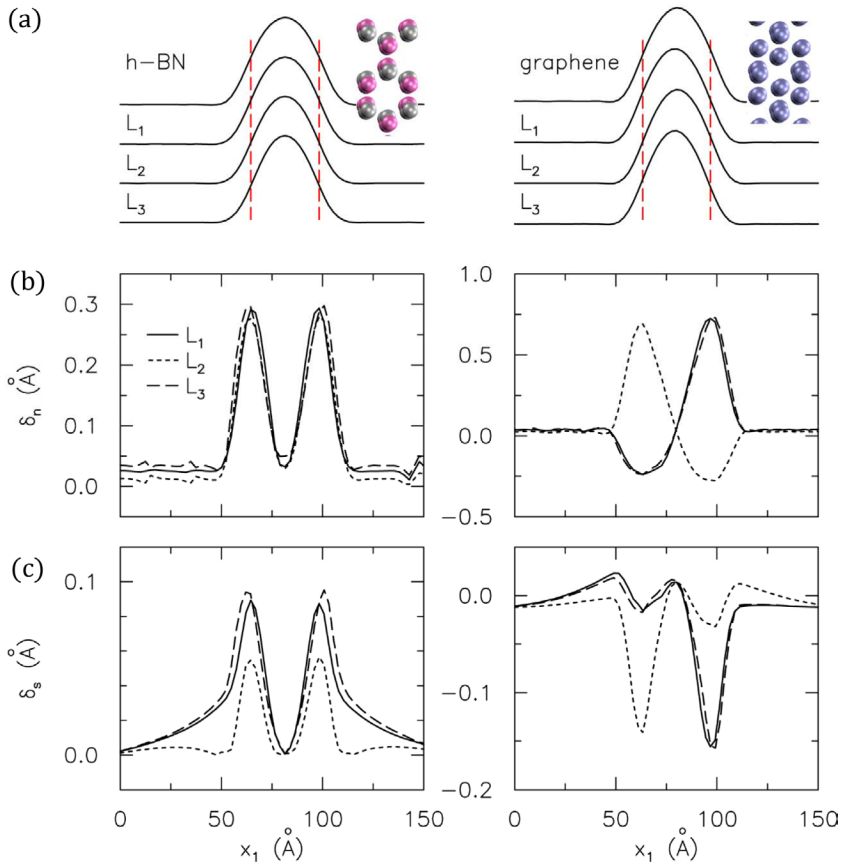

Figure 3. Selected molecular simulation results of deformed few-layer h-BN and graphene. Folded geometries (a), with interlayer normal (b) and shear (c) separations in four-layered h-BN (left) and graphene (right) nanostructures. Insets in (a) display atomic stacking deviations, as viewed from the top, at locations of maximum normal and shear separations indicated by red-dashed lines; pink, grey, and blue denote boron, nitrogen, and carbon atoms, respectively.

2.3. Atomistic simulations of the bending and interlayer shear rigidities of folded BNNS and graphene

To better understand our experimental findings of higher bending and interlayer shear rigidities of BNNS as compared with graphene, we conduct molecular static simulations using the classical MD code LAMMPS. We adopt a recently developed Tersoff parametrization to represent the intra-layer interactions in h-BN, which accurately replicates the strain energy response, equilibrium lattice constant and phonon dispersion relations of BN nanostructures with data from x-ray scattering experiments and density functional theory (DFT) calculations [32, 33]. The intra-layer atomistic interactions between C atoms in graphene are governed by a second-generation reactive empirical bond order (REBO) potential [34], which well describes the bond lengths, bond angles, and dihedral angles in graphene as well as the mechanical (bending) properties [35]. The inter-layer interactions for both graphene and h-BN are described by registry-dependent Kolmogorov–Crespi (KC)-type force fields [36]; this is as opposed to a traditional Lennard–Jones (LJ) type potential which fails to capture the anisotropic effect in short-range repulsion in layered crystalline structures, and can lead to order of magnitude lower sliding energy well depths in comparison with KC results.

We perform stiffness calculations of folded h-BN and graphene sheets, with varying number of interlayers. We construct atomically-flat h-BN and graphene sheets with perfect alternating stable stackings within a periodic simulation cell with in-plane dimensions of $(180 \times 4.3)\,\text{Å}^2$ and $(177 \times 4.3)\,\text{Å}^2$, respectively. We perturb the atomic displacements of the middle third section of these stacked layers to form a 1D sinusoidal wave with an initial displacement amplitude of 5–10 Å in the out-of-plane direction (y-axis) and a half-wave period of 50 Å along one of the in-plane directions (x-axis). The perturbed structure is then energy minimized using the conjugate gradient method, while allowing the box dimensions to relax to achieve zero box pressure in all three directions. The resulting folded structure then corresponds to a local minimum energy state, as exemplified by four-layered h-BN and graphene shown in figure 3(a). For the folded sinusoidal-wave nanostructure with small values of θ (i.e. $\sin\theta \approx \theta$), equation (1) reduces to the expression of the bending stiffness $D_{\text{s/m}} = \frac{F_x}{w^2}$, where F_x is the applied external force along the x-axis and is obtained from virial stress computations of σ_{xx} along the straight-end sections of the h-BN and graphene nanostructures and w is the wave number of the sinusoidal profile fitted to the out-of-plane displacements of the folded nanostructures. We summarize in table 1 the bending stiffness $D_{\text{s/m}}$ of the folded h-BN and graphene nanostructures with one to six stacking layers extracted from our atomistic simulations. Observe

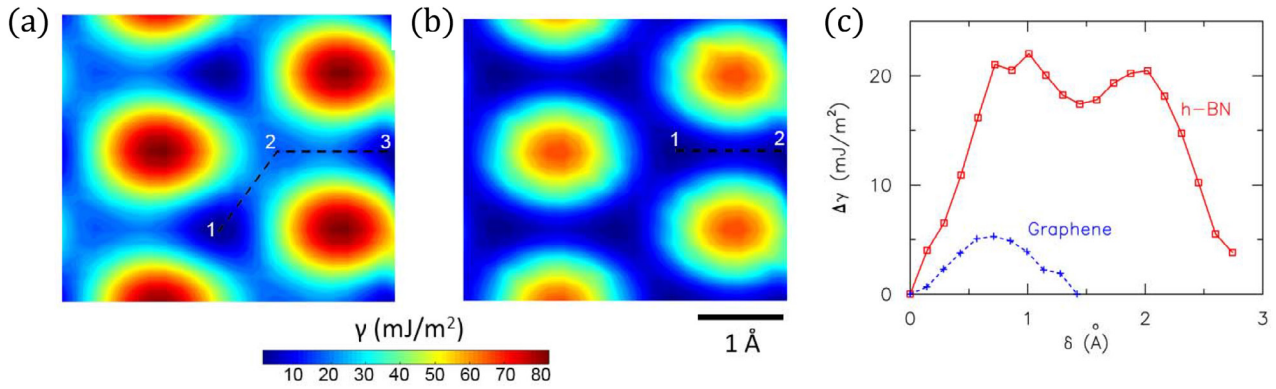

Figure 4. Stacking fault energy contours for h-BN (a) and graphene (b). (c) Change in energy versus displacement for interlayer sliding along the minimum energy pathways outlined by black-dashed lines in (a) and (b).

that the simulation predictions of the bending stiffness are in near-perfect agreement with our experimental measurements for two to six layers of h-BN and graphene.

The bending stiffness of monolayer h-BN and graphene is associated with pure bending of the single atomic layer. In contrast, the stiffness of folded two to six layered h-BN and graphene has added contributions from interlayer sliding and out-of-plane deformation. Figures 3(b) and (c) show the relative change in the normal (δ_n) and shear (δ_s) separations of the three interlayers ($L_1 - L_3$) for the folded 4-layer h-BN and graphene sheets depicted in figure 3(a). Observe that the interlayer deformation (δ_n, δ_s) localizes near the steepest slope of the folded configurations, as marked by red-dashed lines in figure 3(a), and results in significant distortions in the AA′ and AB stacking sequences for h-BN and graphene (insets of figure 3(a)). For h-BN, the relatively stronger binding between interlayers and the higher barrier energies for interlayer sliding result in smaller normal (figure 3(b)) and shear separations (figure 3(c)) compared to graphene. This stronger interlayer interaction explains the consistently higher effective stiffness of folded multilayer h-BN versus graphene (figure 2(b) and table 1), which is in contrast to the lower stiffness of monolayer h-BN versus graphene where the deformation is caused by pure bending. While monolayer graphene has a higher bending stiffness than monolayer h-BN, the higher barrier energy for interlayer sliding and the stronger binding across the interlayers ultimately result in the higher effective stiffness of folded h-BN.

To compute the interlayer shear properties of h-BN and graphene, we adopt periodic, orthogonal simulation cells consisting of dual-layer h-BN and graphene in their energy-minimized state. The respective simulation cells have in-plane dimensions of (17.3×12.5) Å^2 and (17.0×12.3) Å^2, with a 10 nm thick vacuum layer normal to the exposed h-BN and graphene surfaces. We compute the stacking fault energy γ as a function of the interlayer sliding displacements by sliding one h-BN or graphene layer relative to the other along the armchair and zigzag directions. The resulting stacking fault energy surfaces of h-BN and graphene are shown in figures 4(a) and (b), respectively. We indicate with dashed lines the minimum energy pathways for interlayer sliding from one stable AA′ (h-BN) or AB (graphene) stacking arrangement to another, and trace $\Delta\gamma$ along these pathways (figure 4(c)). Our atomistic simulations confirm our experimental observations with a three-fold higher energy barrier for interlayer sliding for h-BN (21.2 mJ m^{-2}) versus graphene (6.9 mJ m^{-2}). These atomistic results are quantitatively in good agreement with prior DFT-obtained sliding barrier energies of 25.7 and 7.9 mJ m^{-2} for h-BN and graphene, respectively [37]. We numerically differentiate $\Delta\gamma$ with respect to the sliding displacement δ along the minimum energy pathways in figure 4(c) to obtain the interlayer shear modulus $G = t_0 \frac{\partial^2 \Delta\gamma}{\partial \delta^2}$ of h-BN (2.34 GPa) and graphene (0.85 GPa) near the equilibrium position (i.e. $\delta \to 0$). These atomistic predictions capture the order of magnitude higher interlayer shear modulus of h-BN (3–4 GPa) versus graphene (~0.4 GPa) observed in our experiments (figure 2(d)). We remark that the atomistic calculations of G are based on perfectly stacked h-BN and graphene layers, and can be considered as upper-bound values. In deformed structures, the barrier energies for interlayer sliding and the corresponding interlayer shear modulus will depend on the presence of stacking imperfections or interlayer dislocations, which are more common in graphene [38, 39] rather than h-BN layers due to the several-fold smaller stacking fault energy of the former (figure 4(c)). This explains the two-fold higher predictions of G for graphene in our simulations as compared to prior studies [9–11, 16]. We have conducted stacking fault energy calculations for tilted commensurate bilayer graphene with a twist angle of $\theta = 46.83°$ measured with respect to AA position, and have confirmed that the presence of this stacking disorder results in much lower interlayer shear modulus values of ~0.23 GPa.

3. Conclusions

In this paper, we investigate the bending deformability of BNNS using a combined experimental-computational approach. Our studies consistently reveal that few-layer BNNS possesses a much higher bending rigidity than comparable graphene, which is attributed to the strong interlayer shear interaction in h-BN. The properties of high bending rigidity and strong interlayer interactions suggest that BNNS is less prone to the interlayer delamination-induced structural inhomogeneities (e.g. shearing, rippling and kinks) that reportedly occur in graphene and enable many of its applications, such

as dielectric substrates for graphene electronics [4] and reinforcing fillers for nanocomposites [40–43]. The high bending rigidity helps to maintain the atomic flatness of thin h-BN, which plays a critical role in the reported superior electron mobilities of graphene electronics. The high interlayer shear rigidity enables superior load carrying capacities of the added fillers and thus enhances the bulk mechanical property of nanocomposites reinforced with multilayer h-BN, while the bulk property of multilayer graphene reinforced nanocomposites might be compromised due to interlayer sliding induced catastrophic failure.

Acknowledgments

This work was supported by the US Air Force Office of Scientific Research—Low Density Materials program under Grant No. FA9550-15-1-0491, and by National Science Foundation under Grant No. CMMI- 1537333 (CK) and CMMI-1538162 (HBC). The atomistic calculations were performed using the computational resources provided by TACC (Award No. TG-MSS130007) and the Blue Waters sustained-petascale computing project, which is supported by the National Science Foundation (Award Nos. OCI-0725070 and ACI-1238993) and the State of Illinois, USA.

ORCID iDs

Changhong Ke https://orcid.org/0000-0002-5170-9859

References

[1] Zhu S and Li T 2014 Hydrogenation-assisted graphene origami and its application in programmable molecular mass uptake, storage, and release *ACS Nano* **8** 2864–72
[2] Becton M, Zhang L and Wang X 2013 Effects of surface dopants on graphene folding by molecular simulations *Chem. Phys. Lett.* **584** 135–41
[3] Zhang L, Zeng X and Wang X 2013 Programmable hydrogenation of graphene for novel nanocages *Sci. Rep.* **3** 3162
[4] Dean C R *et al* 2010 Boron nitride substrates for high-quality graphene electronics *Nat. Nanotechnol.* **5** 722–6
[5] Zhang D-B, Akatyeva E and Dumitrică T 2011 Bending ultrathin graphene at the margins of continuum mechanics *Phys. Rev. Lett.* **106** 255503
[6] Huang Y, Wu J and Hwang K C 2006 Thickness of graphene and single-wall carbon nanotubes *Phys. Rev.* B **74** 245413
[7] Zhang J, Xiao J, Meng X, Monroe C, Huang Y and Zuo J-M 2010 Free folding of suspended graphene sheets by random mechanical stimulation *Phys. Rev. Lett.* **104** 166805
[8] Meng X, Li M, Kang Z, Zhang X and Xiao J 2013 Mechanics of self-folding of single-layer graphene *J. Phys. Appl. Phys.* **46** 055308
[9] Liu Y, Xu Z and Zheng Q 2011 The interlayer shear effect on graphene multilayer resonators *J. Mech. Phys. Solids* **59** 1613–22
[10] Savini G, Dappe Y J, Öberg S, Charlier J-C, Katsnelson M I and Fasolino A 2011 Bending modes, elastic constants and mechanical stability of graphitic systems *Carbon* **49** 62–9
[11] Shen Y and Wu H 2012 Interlayer shear effect on multilayer graphene subjected to bending *Appl. Phys. Lett.* **100** 101909
[12] Lindahl N, Midtvedt D, Svensson J, Nerushev O A, Lindvall N, Isacsson A and Campbell E E B 2012 Determination of the bending rigidity of graphene via electrostatic actuation of buckled membranes *Nano Lett.* **12** 3526–31
[13] Feng X, Kwon S, Park J Y and Salmeron M 2013 Superlubric sliding of graphene nanoflakes on graphene *ACS Nano* **7** 1718–24
[14] Scharfenberg S, Rocklin D Z, Chialvo C, Weaver R L, Goldbart P M and Mason N 2011 Probing the mechanical properties of graphene using a corrugated elastic substrate *Appl. Phys. Lett.* **98** 091908
[15] Tan P H *et al* 2012 The shear mode of multilayer graphene *Nat. Mater.* **11** 294–300
[16] Chen X, Yi C and Ke C 2015 Bending stiffness and interlayer shear modulus of few-layer graphene *Appl. Phys. Lett.* **106** 101907
[17] Guo Y, Qiu J and Guo W 2016 Mechanical and electronic coupling in few-layer graphene and hBN wrinkles: a first-principles study *Nanotechnology* **27** 505702
[18] Pan F, Wang G, Liu L, Chen Y, Zhang Z and Shi X 2019 Bending induced interlayer shearing, rippling and kink buckling of multilayered graphene sheets *J. Mech. Phys. Solids* **122** 340–63
[19] Falin A *et al* 2017 Mechanical properties of atomically thin boron nitride and the role of interlayer interactions *Nat. Commun.* **8** 15815
[20] Qu W, Chen X and Ke C 2017 Temperature-dependent frictional properties of ultra-thin boron nitride nanosheets *Appl. Phys. Lett.* **110** 143110
[21] Gorbachev R V *et al* 2011 Hunting for monolayer boron nitride: optical and Raman signatures *Small* **7** 465–8
[22] García R and San Paulo A 1999 Attractive and repulsive tip-sample interaction regimes in tapping-mode atomic force microscopy *Phys. Rev.* B **60** 4961–7
[23] Paulo Á S and García R 2001 Tip-surface forces, amplitude, and energy dissipation in amplitude-modulation (tapping mode) force microscopy *Phys. Rev.* B **64** 193411
[24] Chen X, Zhang L, Zhao Y, Wang X and Ke C 2014 Graphene folding on flat substrates *J. Appl. Phys.* **116** 164301
[25] Annett J and Cross G L W 2016 Self-assembly of graphene ribbons by spontaneous self-tearing and peeling from a substrate *Nature* **535** 271–5
[26] Hosseini M, Gorgani H H, Shishesaz M and Hadi A 2017 Size-dependent stress analysis of single-wall carbon nanotube based on strain gradient theory *Int. J. Appl. Mech.* **09** 1750087
[27] Hosseini M, Hadi A, Malekshahi A and Shishesaz M 2018 A review of size-dependent elasticity for nanostructures *J. Comput. Appl. Mech.* **49** 197–211
[28] Yu M-F, Kowalewski T and Ruoff R S 2001 Structural analysis of collapsed, and twisted and collapsed, multiwalled carbon nanotubes by atomic force microscopy *Phys. Rev. Lett.* **86** 87–90
[29] Hsing C-R, Cheng C, Chou J-P, Chang C-M and Wei C-M 2014 van der Waals interaction in a boron nitride bilayer *New J. Phys.* **16** 113015
[30] Chopra N G, Benedict L X, Crespi V H, Cohen M L, Louie S G and Zettl A 1995 Fully collapsed carbon nanotubes *Nature* **377** 135–8
[31] Lebedev A V, Lebedeva I V, Knizhnik A A and Popov A M 2016 Interlayer interaction and related properties of bilayer hexagonal boron nitride: *ab initio* study *RSC Adv.* **6** 6423–35
[32] Kınacı A, Haskins J B, Sevik C and Çağın T 2012 Thermal conductivity of BN-C nanostructures *Phys. Rev.* B **86** 115410

[33] Sevik C, Kinaci A, Haskins J B and Çağın T 2011 Characterization of thermal transport in low-dimensional boron nitride nanostructures *Phys. Rev.* B **84** 085409
[34] Brenner D W, Shenderova O A, Harrison J A, Stuart S J, Ni B and Sinnott S B 2002 A second-generation reactive empirical bond order (REBO) potential energy expression for hydrocarbons *J. Phys.: Condens. Matter* **14** 783
[35] Lu Q, Arroyo M and Huang R 2009 Elastic bending modulus of monolayer graphene *J. Phys. D: Appl. Phys.* **42** 102002
[36] Ouyang W, Mandelli D, Urbakh M and Hod O 2018 Nanoserpents: graphene nanoribbon motion on two-dimensional hexagonal materials *Nano Lett.* **18** 6009–16
[37] Zhou S, Han J, Dai S, Sun J and Srolovitz D J 2015 van der Waals bilayer energetics: generalized stacking-fault energy of graphene, boron nitride, and graphene/boron nitride bilayers *Phys. Rev.* B **92** 155438
[38] Butz B, Dolle C, Niekiel F, Weber K, Waldmann D, Weber H B, Meyer B and Spiecker E 2014 Dislocations in bilayer graphene *Nature* **505** 533–7
[39] Brown L, Hovden R, Huang P, Wojcik M, Muller D A and Park J 2012 Twinning and twisting of tri- and bilayer graphene *Nano Lett.* **12** 1609–15
[40] Zhi C, Bando Y, Tang C, Kuwahara H and Golberg D 2009 Large-scale fabrication of boron nitride nanosheets and their utilization in polymeric composites with improved thermal and mechanical properties *Adv. Mater.* **21** 2889–93
[41] Kiran M S R N, Raidongia K, Ramamurty U and Rao C N R 2011 Improved mechanical properties of polymer nanocomposites incorporating graphene-like BN: dependence on the number of BN layers *Scr. Mater.* **64** 592–5
[42] Nam S, Chang K, Lee W, Kim M J, Hwang J Y and Choi H 2018 Structural effect of two-dimensional BNNS on grain growth suppressing behaviors in Al-matrix nanocomposites *Sci. Rep.* **8** 1614
[43] Tatarko P, Grasso S, Porwal H, Chlup Z, Saggar R, Dlouhý I and Reece M J 2014 Boron nitride nanotubes as a reinforcement for brittle matrices *J. Eur. Ceram. Soc.* **34** 3339–49